Nuclear Engineering and Design 429 (2024) 113560

Contents lists available at ScienceDirect

Nuclear Engineering and Design

journal homepage: www.elsevier.com/locate/nucengdes

An efficient method for input uncertainty propagation in CFD and the application to buoyancy-driven flows

Ruiyun Ji [a,b,*], Stephan Kelm [b], Markus Klein [a]

[a] University of the Bundeswehr Munich, Institute of Applied Mathematics and Scientific Computing (LRT-1), Neubiberg, Germany
[b] Forschungszentrum Juelich GmbH, Institute of Energy Technologies (IET-4), Juelich, Germany

ARTICLE INFO

Keywords:
Input uncertainty propagation
Deterministic sampling

ABSTRACT

Severe accident scenarios address the release of large amounts of hydrogen and steam to the containment. The formation of a flammable gas cloud could lead to a combustion and even failure of containment structures. In order to support the hydrogen mitigation method development, a detailed understanding of the gas transport and mixing process is crucial. Efforts in terms of numerical simulations such as Computational Fluid Dynamics (CFD) models have been made, which allow to investigate the complex 3D gas mixing process. One of the uncertainty sources that challenge the reliability of CFD validation results is the input uncertainty. It was assessed efficiently using the deterministic sampling method, which requires e.g., in the present case only eight binary samples for seven uncertain input parameters. However, the lean number of samples makes the direct derivation of a probability density function as well as a 95% confidence interval impossible. The assumption of a normal distribution does not always yield convincing and physically consistent output uncertainty bands, in particular for measurements inherent to oscillations. In this context, a new method has been proposed, which enables the generation of reasonable pseudo-samples without additional CFD simulations and the derivation of 95% confidence interval through the statistical analysis on these pseudo-samples. It was assessed against the Monte Carlo sampling method with a simple test case and confirmed an improved prediction. This method has been applied to the large scale application-oriented validation case THAI-TH32 in this work, in order to assess the impact of input uncertainties on the CFD results.

1. Introduction

The severe reactor accident in Fukushima (2011) reminds of the importance of maintaining the integrity of the containment. As a consequence of the accumulation of a flammable hydrogen–air–steam mixture inside a reactor containment or connected buildings, a hydrogen explosion can damage the structures or safety systems and thus lead to a release of radioactive material into the environment. In order to understand the flow and gas transport process in the containment, efforts in terms of experiments for thermal-hydraulic phenomena and numerical simulations have been made. The first one, such as THAI series experiments (Gupta et al., 2015), provides a database, while the latter one utilizes models to investigate the complex 3D flow in complicated geometry, for instance the tailored *containmentFOAM* CFD package (Kelm et al., 2021).

As discussed by Kelm et al. (2016), CFD simulations for the natural circulation mixing experiment THAI-TH22 revealed considerable sensitivity to the initial and boundary conditions. The sensitivity poses challenges to the reliability of model validation and safety relevant CFD applications. Motivated by the previous work, the impact of initial and boundary conditions is further investigated with the repetition experiment THAI-TH32 (Freitag et al., 2022a,b).

The CFD simulation is subject to various uncertainties, i.e., numerical , model and input uncertainties. According to their characteristics and following the Best Practice Guidelines (Mahaffy et al., 2015), they are handled with different approaches. The numerical and model uncertainties have been assessed in Wenig et al. (2021), Ji et al. (2023), and will not be further discussed in this work. The input uncertainties are related to physical properties, initial and boundary conditions, which are usually defined from experimental data and measured with uncertainty. It is presumed that a prior knowledge about input uncertainty is available and the input parameters are assigned with density functions. Hence, the resulting uncertainty is assessed in a probabilistic framework by input uncertainty propagation methods.

The uncertainty propagation methods include sampling approaches (e.g., Monte Carlo sampling (MC) (Pisaroni, 2017) and deterministic sampling (DS) (Hessling, 2013; Julier and Uhlmann, 2004; Angrisani

* Corresponding author at: University of the Bundeswehr Munich, Institute of Applied Mathematics and Scientific Computing (LRT-1), Neubiberg, Germany.
E-mail address: r.ji@fz-juelich.de (R. Ji).

https://doi.org/10.1016/j.nucengdes.2024.113560
Received 16 February 2024; Received in revised form 24 June 2024; Accepted 20 August 2024
Available online 10 September 2024

Nomenclature

μ	mean value
$\mu_{t,t_j}, \sigma_{t,t_j}$	mean value and standard deviation of the times describing the physical state at t_j in different realizations
$\mu_{y,t_j}, \sigma_{y,t_j}$	mean value and standard deviation of the output values describing the physical state at t_j in different realizations
σ	standard deviation
N	number of uncertain input parameters
n	sample size
t_j	a point in time describing a specific physical state of a transient process
$t_{\mathbf{X_i},t_j}$	the ith realization of the times describing the physical state at t_j with the sample $\mathbf{X_i}$
$y_{\mathbf{X_i},t_j}$	the ith realization of the output values describing the physical state at t_j with the sample $\mathbf{X_i}$
Y_{ref}	a predefined output quantity used to determine $t_{\mathbf{X_i},t_j}$

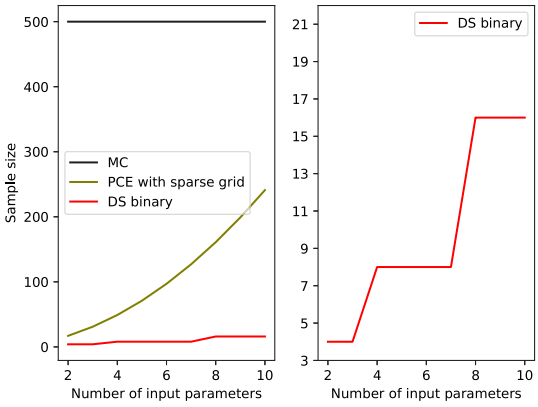

Fig. 1. The sample size with three UQ methods: MC, PCE and DS (left), the DS binary samples corresponding to the number of input parameters (right). The input parameters are assumed following uniform distributions. With the MC method, 500 samples are utilized to obtain 99th percentile value with a confidence level 95% (Glaeser, 2008). For the PCE, the sample size reduces e.g. by using a sparse grid level of two. The binary sample set is one specific DS ensemble and its sample size is determined with the formula $2^{ceil(\frac{N+5}{4})}$ (Hessling, 2013), where N is the number of input parameters.

et al., 2005)) and surrogate models (e.g., polynomial chaos expansion (PCE) and Gaussian process models (Smith, 2013)). With the MC sampling method, the sample size does not depend on the number of input parameters but on the targeted accuracy (Glaeser, 2008). It converges slowly and the required number of samples is high for a dedicated assessment. With the surrogate model method, a meta-model is constructed from a reduced number of CFD simulations, describing the output quantity of interest as a function of uncertain input parameters. The method is efficient for a low number of input parameters, however suffers from the curse of dimensionality. In order to reduce the sample size, different efforts have been made, for instance the application of the Quasi-Monte Carlo method, deterministic sampling method or various efficient sampling strategies for the surrogate model method (Smith et al., 2015; Blatman and Sudret, 2011). The DS approach becomes attractive because of its comparatively lean number of samples, as depicted in Fig. 1.

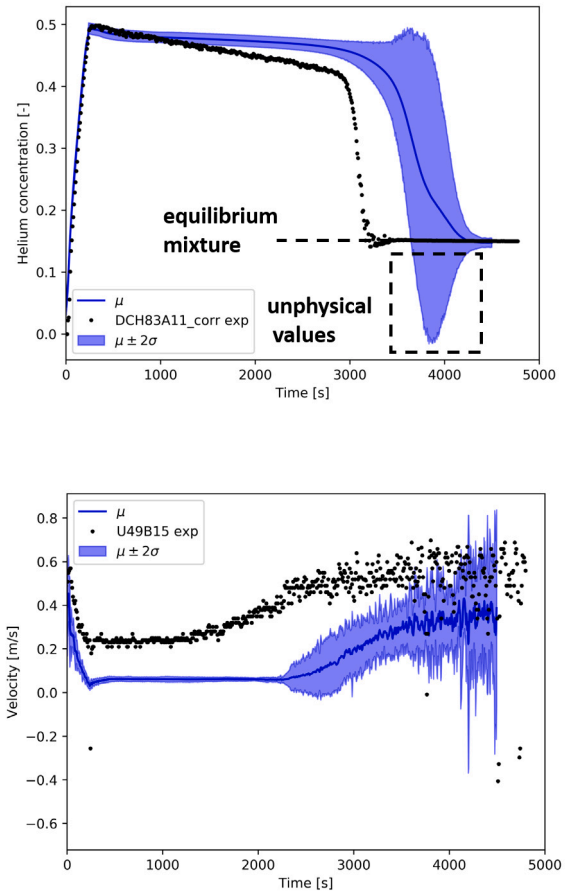

Fig. 2. The simulation results represent the evolution of the helium volume concentration in the dome (upper) and the velocity in the annulus (bottom) and their measurements of the experiment TH32 (Freitag et al., 2022b), which is detailed in Section 4. The uncertainty bands are obtained with the expression $\mu \pm 2\sigma$.

The method has been also applied to nuclear reactor safety applications and proved its good performance (Rakhimov et al., 2019; Wang and Ma, 2023). Thus, it is further investigated in the current work.

Independent of the chosen sample set, the DS method cannot represent entire probability density functions (PDFs) but encodes the statistical moments correctly up to a certain order. As output statistics, the mean, variance and further statistical moments are computed with DS samples. To derive the output uncertainty band, additional assumption for the PDF of an output quantity is required. As a common approach, a normal distribution is assumed and the output uncertainty band is expressed as $\mu \pm 2\sigma$ (two times the standard deviation around the mean value). However, this can lead to an envelope of unphysical values, such as negative gas concentration and smaller values than the one in the equilibrium mixture (Fig. 2 upper subplot). In addition, due to small number of samples, the oscillation effect inherent to parameters will further impact the output uncertainty, yielding strongly fluctuating uncertainty bands, as shown in Fig. 2 bottom subplot.

The objective of this work is to develop a method that appropriately estimates the uncertainties by applying the DS sampling methodology to challenging transient test cases. This includes the evaluation of the confidence intervals which is beyond the standard outputs of the DS method. Additionally, this method should be applicable to the technical scale case TH32 while maintaining affordable computational costs.

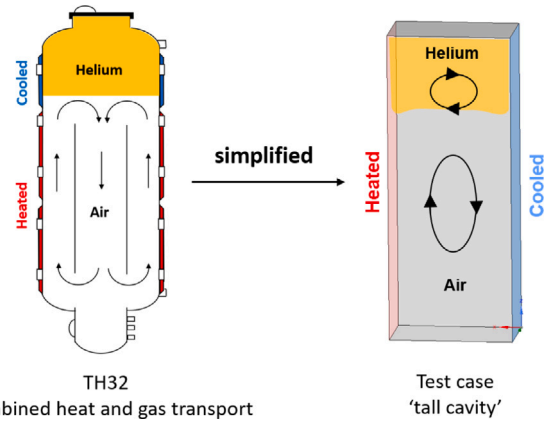

Fig. 3. The application THAI-TH32 (left) and the scaled and idealized test case 'tall cavity' (right).

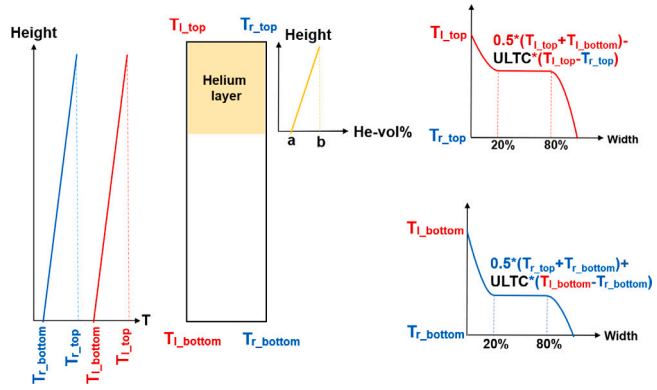

Fig. 4. 'Tall cavity' and its initial and boundary conditions.

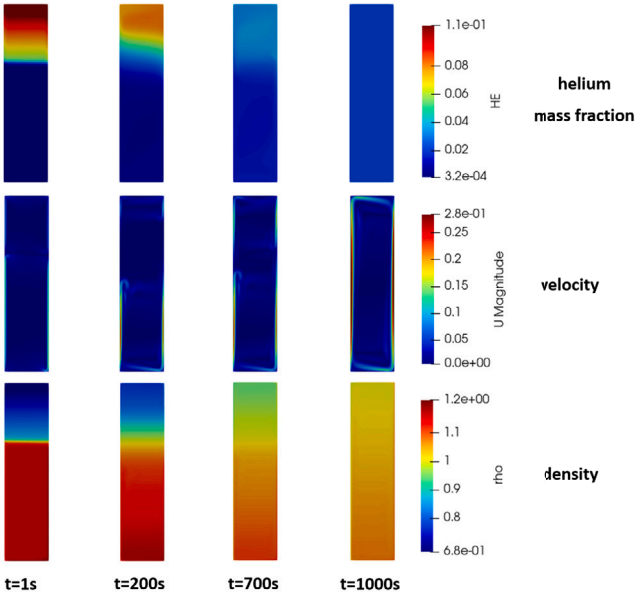

Fig. 5. The evolution of the helium mass fraction, velocity and density during the mixing process at different times.

2. Method development

2.1. A simplified test case 'tall cavity'

During the method development, because of the high computing cost for the technical scale validation case THAI-TH32 (Freitag et al., 2022a,b), the simplified test case 'tall cavity' has been introduced, as shown in Fig. 3. To ensure the scalability to the TH32 application, it must preserve essential boundary conditions (such as the cooled and heated structures) and capture similar physics as in the TH32 configuration. The intensity of the fundamental natural circulation flow is characterized by the Rayleigh number (Ra, with the value $2 \cdot 10^9$ in the current case). In addition, the mixing process for gases helium and air is simulated by initially defining a helium layer in the upper third of the cavity. Furthermore, the geometry of the simplified test case should enable a simple and obvious comparison of results to support the method development.

The 'tall cavity' has an aspect ratio of four with the height 1 m and width 0.25 m. The initial and boundary conditions for the walls are illustrated in Fig. 4. Fixed temperature profiles are imposed on the vertical and horizontal walls. The vertical walls are defined with linearly ascending or uniform temperature profiles along the height, in analogy to the wall temperature observed in the TH32. The horizontal walls are imprinted by combined temperature profiles, i.e. the uniform temperatures in the middle and parabolic profiles at the ends, as shown in the right side of Fig. 4. Additionally, a factor $ULTC$ (Upper and Lower Temperature Coefficient) is introduced for the definition of uniform temperatures, keeping them between the temperatures at the ends. The entire cavity is filled with air and contains a helium layer with upwards increasing volume fraction in the upper section. The average value of the helium volume fraction is 40%. During the mixing process, the helium layer is remobilized by the buoyancy driven flow induced by the heated and cooled walls.

The mixing process driven by natural circulation flows is illustrated in Fig. 5. The heated/cooled walls induce buoyancy-driven flow in the cavity. The presence of the helium stratification, and consequently the lower density in the upper part of the cavity, prevents the establishment of the global natural circulation flow (as observed at $t = 1000$ s). However, two flow loops can be identified below and in the helium layer (such as at $t = 200$ s and 700 s), with the flow at the lower part revealing higher velocities. The helium is transported and mixed with air mainly through the flow in the lower part. During the mixing process, the flow keeps developing, starting with a gradual increase in velocity and then transitioning to a rapid increase. As the helium concentration tends to be homogeneous, a global natural circulation flow with high velocities is established, and the atmosphere in the cavity reaches an equilibrium state.

2.2. Method description

Fig. 6 illustrates exemplarily the realizations of a velocity in the cavity for various initial and boundary conditions, when the MC and DS approaches are used for the input uncertainty propagation.

Because of the high sample size for the MC method, it is possible to directly derive the PDF or cumulative density function (CDF) and the 95% confidence interval through statistical analysis. However, it is impossible for the DS approach with the small number of samples.

From Fig. 6, a common feature of the outcomes is identified, i.e., they have similar profiles which are shifted both in time and value. For instance, Fig. 7 displays the transition points where the vertical velocity rapidly increases. The variation in time and output value is presented by the points in two-dimension, with 500 and eight points for the MC and DS methods, respectively.

As the DS samples encode some of the statistical information about the input uncertainty, its outcomes are assumed to capture some crucial features similar to the MC samples. Based on the DS outcomes, it is then intended to generate more reasonable pseudo-points that hold the essential features and are expected to be comparable with the MC ones

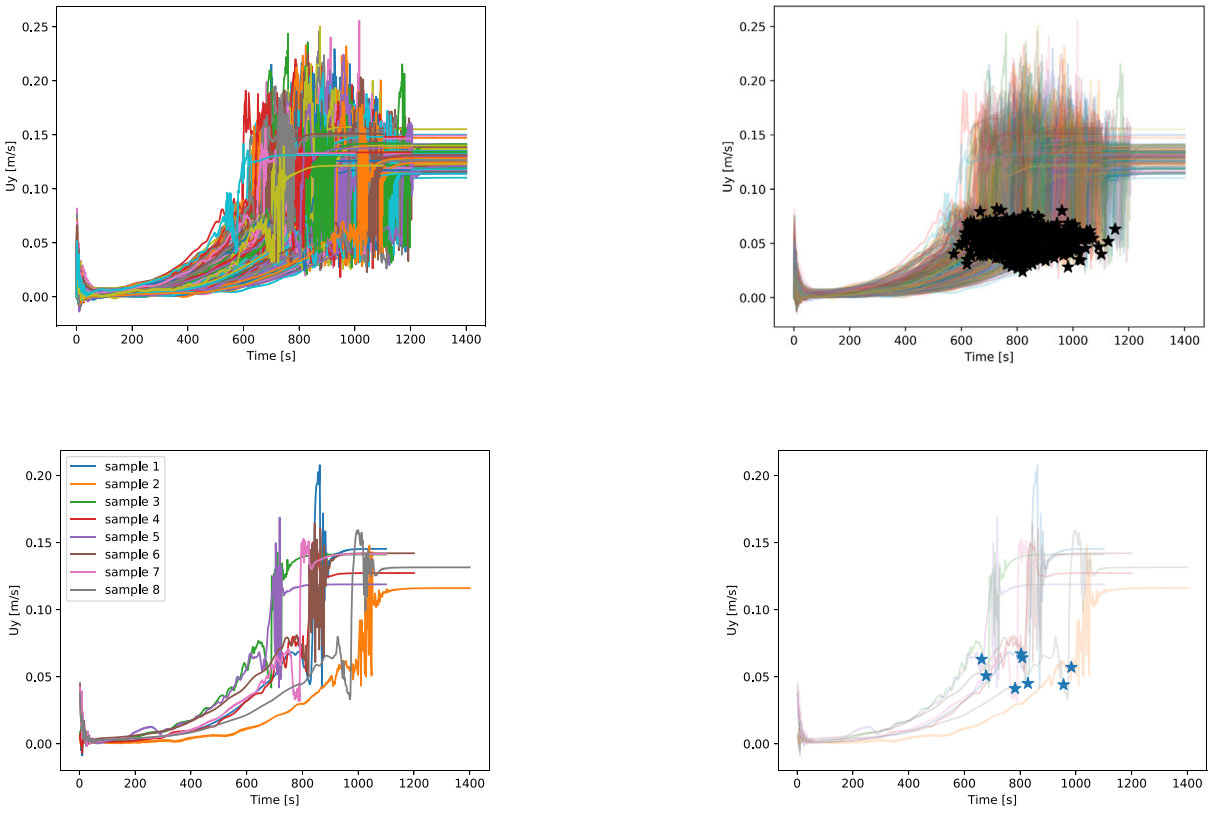

Fig. 6. The outcomes of the velocity with vertical component at the location (0.015 0.8 0.005) for the test case with 500 MC samples (upper) and 8 DS samples (bottom).

Fig. 7. The transition points of the vertical velocity determined from 500 MC samples (upper) and 8 DS samples (bottom).

(Fig. 8). In this way, the derivation of CDF and 95% confidence interval through the statistical analysis on these pseudo-outcomes is possible. Developing a methodology to realize the concept, is the main focus of the study.

The characteristic variation (both in time and output value) is addressed by calculating the mean values and variances of the time and output values, respectively. For example, the statistics at the point in time t_j of the transient process are determined with the expressions:

$$\mu_{t,t_j} = \frac{1}{n}\sum_{i=1}^{n} t_{\mathbf{X_i},t_j}, \tag{1}$$

$$\mu_{y,t_j} = \frac{1}{n}\sum_{i=1}^{n} y_{\mathbf{X_i},t_j}, \tag{2}$$

$$\sigma^2_{t,t_j} = \frac{1}{n-1}\sum_{i=1}^{n} (t_{\mathbf{X_i},t_j} - \mu_{t,t_j})^2, \tag{3}$$

$$\sigma^2_{y,t_j} = \frac{1}{n-1}\sum_{i=1}^{n} (y_{\mathbf{X_i},t_j} - \mu_{y,t_j})^2. \tag{4}$$

$t_{\mathbf{X_i},t_j}$ and $y_{\mathbf{X_i},t_j}$ indicate the resulting time and output value for an output quantity y with the sample $\mathbf{X_i}$ at the time t_j. μ_{t,t_j} and μ_{y,t_j} are the mean values for the time and output quantity, σ^2_{t,t_j} and σ^2_{y,t_j} stand for their variances.

By making assumptions for the PDFs of the time and output value (explained in Section 2.3) and combining the two PDFs, more pseudo-samples in two-dimension can be generated as the possible outcomes of the output parameter at the time t_j. As illustrated in Fig. 9 upper, three sample ensembles are generated based on the evaluation at the times

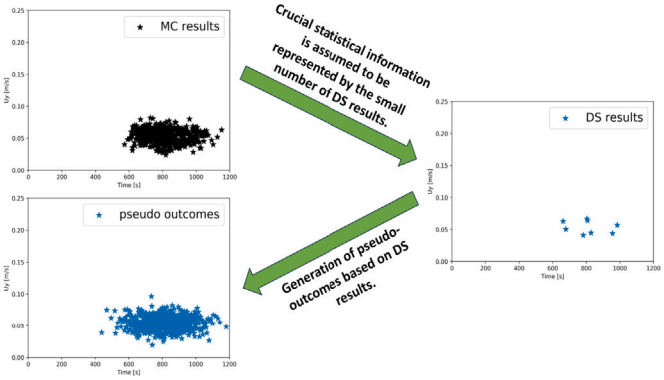

Fig. 8. Conceptual idea behind the method development.

700 s, 800 s and 900 s. For the transient process, all pseudo-points are then available, as shown in Fig. 9 bottom. Based on them, the possible outcomes at each point in time (which are from different ensembles and indicated by different colors) are collected. By performing statistical analysis on the collected outcomes, the CDF and the 95% confidence interval are derived (explained in Appendix A).

2.3. Method realization

The first step of the previously described method is to determine the times and values in variation, i.e., $t_{\mathbf{X_i},t_j}$ and $y_{\mathbf{X_i},t_j}$ at each evaluated time t_j, as shown in Fig. 7 bottom. For the proposed method, $t_{\mathbf{X_i},t_j}$ are

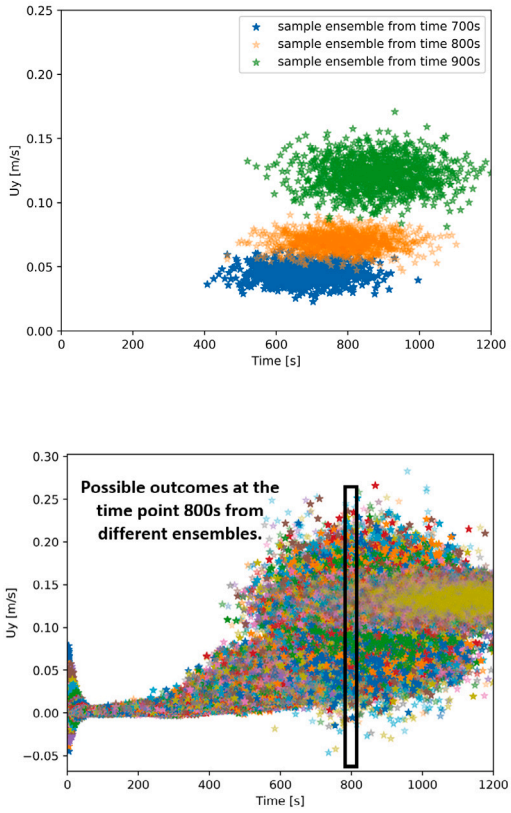

Fig. 9. (Upper) the generated pseudo-samples based on the evaluation for times 700 s, 800 s and 900 s, (bottom) the sample ensembles for all evaluated times and the statistical analysis for the time 800 s.

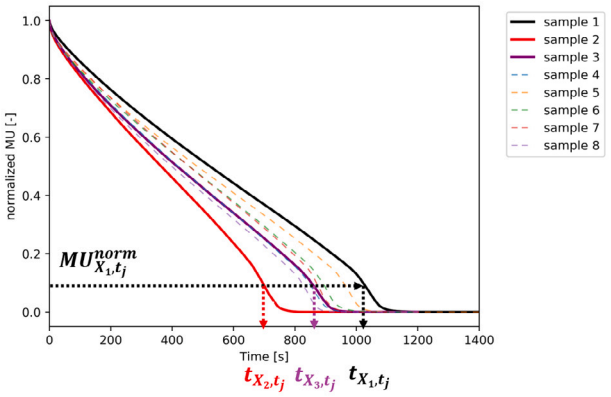

Fig. 10. The determination of different times indicating a specific physical state with the normalized MU.

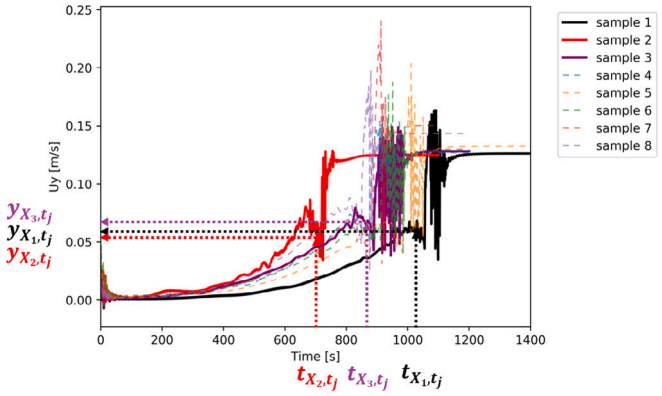

Fig. 11. The determination of different velocities with times.

determined first and $y_{\mathbf{X}_1,t_j}$ afterwards. The mapping can be done based on a monotonically increasing or decreasing profile which represents similar physical states of the system (Wenig et al., 2023). For this reason, the parameter mixture uniformity (MU) is introduced with the expression:

$$MU = \sqrt{\frac{1}{V}\int_V (X_{HE} - X_{equ})^2 \mathrm{d}V}, \tag{5}$$

where X_{HE} is the volume fraction of helium in each cell and X_{equ} the helium volume fraction at the equilibrium state. The value of MU is high in the presence of a helium stratification and tends to zero during the mixing process.

Through the normalization (subtracting the minimal value and then dividing by the maximum one), the values of MU are bounded between 0 and 1, as shown in Fig. 10. The lines with different colors indicate the normalized MU profiles for all the DS samples. As indicated by the arrows, the same output value $MU^{norm}_{\mathbf{X}_1,t_j}$ corresponds to different times. In other words, the variation in time is determined by a predefined output value of a suitable quantity, e.g. MU. Afterwards, by mapping these times back to the QoI (such as the vertical velocity in Fig. 11), the variation in output quantity is obtained.

The previous procedure is carried out for all evaluated points in time, corresponding to the written transient data points of the simulation result. In terms of predefined output values, a reference case (the sample 1 in the study) is selected. Its normalized MU at selected points in time are the predefined output values.

The times and output values are assumed to follow normal distributions, which has been verified through the Shapiro–Wilk test with eight DS samples (Shaphiro and Wilk, 1965). As criterion for rejecting the hypothesis, a p-value smaller than 5% was adopted (Dudley, 2012). Since the p-values are found generally higher than 5%, the normal distributions were deployed for the current case. It should be noted that the assumption for PDFs is not limited to the normal distribution, further possibilities (such as the log-normal, Weibull distributions, etc.) can be considered and verified for a general application.

The features of the DS results are quantitatively described by normal distributions with their statistics computed from Eqs. (1) to (4). As aforementioned, the pseudo-outcomes will be generated and the statistical analysis can be performed.

3. Method assessment

3.1. Numerical setup for the test case

The solver *containmentFluidFoam* (Kelm et al., 2021) with the URANS approach is applied to calculate the flow and gas transport processes. The governing equations for the mass, momentum, energy and gas species transport are explained in Kelm et al. (2021). They are closed by adopting the $k-\omega$ Shear Stress Transport model (SST-2003 (Menter et al., 2003)) with two additional equations. In particular, the buoyancy effect on turbulence has been identified as critical (Abe et al., 2015), thus two source terms are included in the $k-\omega$ SST turbulence model to account for the production and

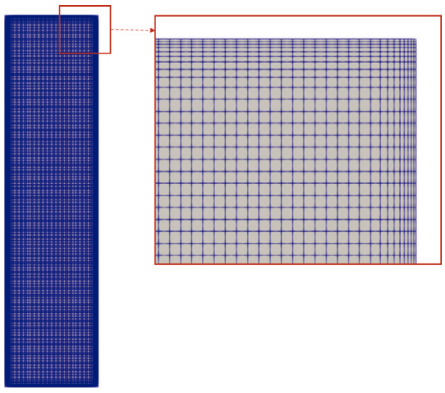

Fig. 12. The mesh used for the test case.

dissipation of the turbulence due to buoyancy forces (Kelm et al., 2021). The buoyancy effects are caused by the density changes and described by a full density-based buoyancy model.

Second-order accurate numerical schemes were utilized. The numerical uncertainty has been minimized by addressing the iteration, temporal and spatial discretization errors. The iterative error was minimized by applying strict convergence criteria, i.e., the tolerance value 10^{-5} for the solvers and the outer corrector residual 10^{-4} for the PIMPLE-loop. The time step was determined through a time step sensitivity analysis based on the finest mesh and the one with a maximum CFL number of 0.5 has been chosen. Furthermore, the spatial discretization error was addressed by a mesh study with the Least Squares Method (Eça and Hoekstra, 2014). The mesh with 36,146 cells and $y^+ < 0.2$ yielded negligible discretization error and was used for further UQ analysis (Fig. 12).

3.2. Results

Seven uncertain input parameters are defined for UQ, as listed in Table 1. The parameter WTD (Wall Temperature Difference) denotes the temperature difference between the heated and cooled vertical walls, WTG (Wall Temperature Gradient) indicates the temperature change along the vertical walls. The parameter HE (Helium distribution) means the gradient of the helium layer. With the parameter $ULTC$ (Upper and Lower Temperature Coefficient), the temperature profiles at the upper and lower horizontal walls are defined as illustrated in Fig. 4. The parameters D, η and Pr stand for the binary diffusion coefficient of helium in air, the initial dynamic viscosity and the Prandtl number of the dominant species air.

It is assumed that the seven input parameters are independent. The input uncertainties of the first four are characterized by the truncated normal distributions $tN(\mu, \sigma, x_{low}, x_{up})$. Their PDFs are defined as below (Pisaroni, 2017):

$$P(x) = \begin{cases} 0 & \text{for } x < x_{low} \\ \frac{1}{z}\frac{1}{\sqrt{2\pi}\sigma} e^{\frac{-(x-\mu)^2}{2\sigma^2}} & \text{for } x_{low} \le x \le x_{up},\ with\ z = \int_{x_{low}}^{x_{up}} \frac{1}{\sqrt{2\pi}\sigma} e^{\frac{-(x-\mu)^2}{2\sigma^2}} \mathrm{d}x \\ 0 & \text{for } x > x_{up}\ . \end{cases} \tag{6}$$

The mean values of the truncated normal distributions refer to the values in the second column of Table 1 (denoted as r), and the standard deviations are equal to the mean values multiplied by different factors. The lower and upper limits, x_{low} and x_{up}, are defined in the same way. The remaining three physical properties are characterized by uniform distributions with the lower and higher limits specified with $+/-20\%$ deviations to their reference values. It must be noted that the standard deviations σ in Eq. (6) and Table 1 are identical with the original

Table 1
Input parameters and uncertainties for the case with Ra=$2 \cdot 10^9$.

Quantity	Reference (r)	Uncertainty
WTD	21.43 [K]	$tN(r, 10\%r, 80\%r, 120\%r)$
WTG	3.21 [K/m]	$tN(r, 50\%r, 0, 200\%r)$
HE	48.5 [%/m]	$tN(r, 50\%r, 0, 200\%r)$
$ULTC$	0.2 [–]	$tN(r, 50\%r, 0, 200\%r)$
D	$6.9045 \cdot 10^{-5}$ [m^2/s]	$U(80\%r, 120\%r)$
η	$1.845 \cdot 10^{-5}$ [kg/(m s)]	$U(80\%r, 120\%r)$
Pr	0.70745 [–]	$U(80\%r, 120\%r)$

Table 2
The binary sample ensemble for the test case with seven uncertain parameters.

Quantity	Sample 1	Sample 2	Sample 3	Sample 4
WTD	$\mu_1 + \sigma_1$	$\mu_1 - \sigma_1$	$\mu_1 + \sigma_1$	$\mu_1 - \sigma_1$
WTG	$\mu_2 + \sigma_2$	$\mu_2 + \sigma_2$	$\mu_2 - \sigma_2$	$\mu_2 - \sigma_2$
HE	$\mu_3 + \sigma_3$	$\mu_3 + \sigma_3$	$\mu_3 + \sigma_3$	$\mu_3 + \sigma_3$
ULT	$\mu_4 - \sigma_4$	$\mu_4 + \sigma_4$	$\mu_4 + \sigma_4$	$\mu_4 - \sigma_4$
D	$\mu_5 - \sigma_5$	$\mu_5 - \sigma_5$	$\mu_5 + \sigma_5$	$\mu_5 + \sigma_5$
η	$\mu_6 + \sigma_6$	$\mu_6 - \sigma_6$	$\mu_6 + \sigma_6$	$\mu_6 - \sigma_6$
Pr	$\mu_7 - \sigma_7$	$\mu_7 + \sigma_7$	$\mu_7 + \sigma_7$	$\mu_7 - \sigma_7$
Quantity	Sample 5	Sample 6	Sample 7	Sample 8
WTD	$\mu_1 + \sigma_1$	$\mu_1 - \sigma_1$	$\mu_1 + \sigma_1$	$\mu_1 - \sigma_1$
WTG	$\mu_2 + \sigma_2$	$\mu_2 + \sigma_2$	$\mu_2 - \sigma_2$	$\mu_2 - \sigma_2$
HE	$\mu_3 - \sigma_3$	$\mu_3 - \sigma_3$	$\mu_3 - \sigma_3$	$\mu_3 - \sigma_3$
ULT	$\mu_4 - \sigma_4$	$\mu_4 + \sigma_4$	$\mu_4 + \sigma_4$	$\mu_4 - \sigma_4$
D	$\mu_5 + \sigma_5$	$\mu_5 + \sigma_5$	$\mu_5 - \sigma_5$	$\mu_5 - \sigma_5$
η	$\mu_6 - \sigma_6$	$\mu_6 + \sigma_6$	$\mu_6 - \sigma_6$	$\mu_6 + \sigma_6$
Pr	$\mu_7 + \sigma_7$	$\mu_7 - \sigma_7$	$\mu_7 - \sigma_7$	$\mu_7 + \sigma_7$

normal distribution without truncation. However, the actual standard deviation of the truncated normal distribution is smaller and is further considered to determine the DS samples.

According to the PDFs, eight binary samples were generated as in Table 2. As the QoI, the volume-averaged kinetic energy E_{kin} (Eq. (7)), measuring the flow in the tall cavity, has been evaluated.

$$E_{kin} = \frac{1}{V}\int_V \frac{1}{2}(U_x^2 + U_y^2 + U_z^2)\,\mathrm{d}V\,, \tag{7}$$

with U_x, U_y and U_z indicating the velocity components. The capability of the proposed method to handle the point-wise data has been assessed through the test case, for example by evaluating the velocity with its vertical component and the helium concentration measured at the locations (0.015 0.8 0.005) and (0.125 0.80 0.005), respectively.

The times and outcomes in variation were obtained as the method described in Section 2.3. The assumption, that the time and output value follow normal distributions, has been examined with the Shapiro–Wilk test for all QoIs. As exemplarily exhibited in Fig. 13, p-values are found to be considerably higher than 5%, thus the hypothesis of normal distributions has been adopted.

As the required information about the normal distributions for the time and output value was available, sample ensembles for the evaluated times were generated. Afterwards, the relevant samples were collected to derive the CDFs and 95% confidence intervals.

As depicted in both upper subplots of Fig. 14, the bands with different colors represent the 95% confidence intervals derived with different methods, their lower and upper bounds correspond to the CDFs with probabilities of 2.5% and 97.5%, respectively. The dash-dotted, solid and dotted lines within areas present the output values with cumulative probabilities 25%, 50% and 75%.

In contrast to the original method (blue), the proposed approach (red) yields output values with comparable cumulative probabilities to the MC reference (black). In addition, the 95% confidence intervals derived from the proposed method do not include unphysical values (such as negative values of E_{kin}), and they are in good agreement with the intervals obtained with the MC method. This can be explained by

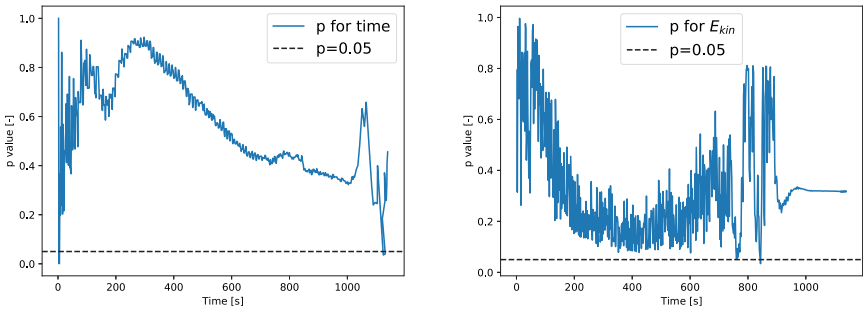

Fig. 13. The p-values for time (left) and E_{kin} (right) with $Ra = 2 \cdot 10^9$.

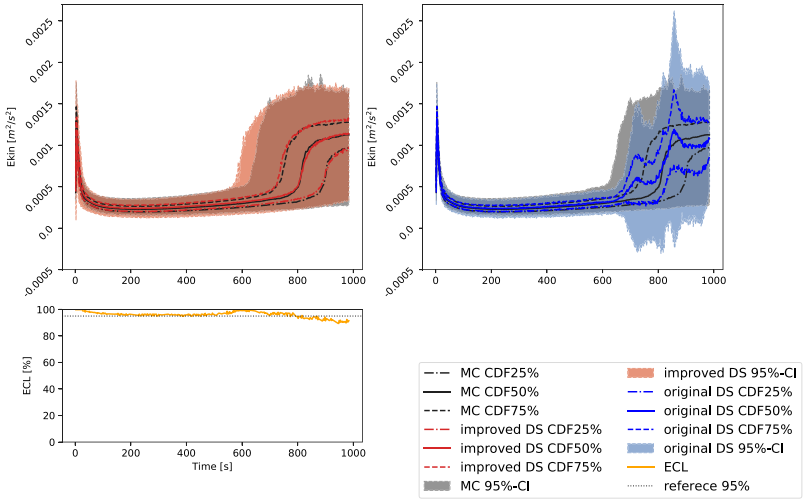

Fig. 14. The 95% confidence intervals and values of E_{kin} with cumulative probabilities 25%, 50% and 75% obtained with the proposed method (upper left) and the original approach (upper right), both are assessed against the MC results. The evaluation of the 95% confidence intervals obtained with the proposed method by calculating the ECL (bottom left).

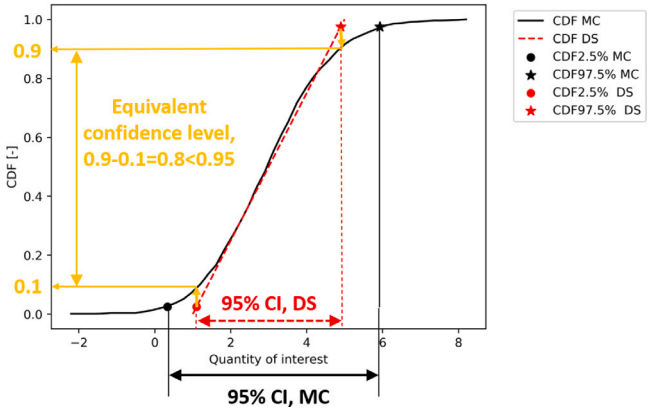

Fig. 15. An example illustrates the CDFs derived from the MC and DS methods, with the assumptions that the MC results follow a normal distribution and the DS results follow a uniform distribution, and the evaluation of the DS confidence interval (CI) by calculation of the ECL.

the comparable CDFs derived with the MC and the proposed method, as shown in Fig. B.28 in Appendix B. Concluding, the 95% confidence interval derived with the novel method is more realistic.

The 95% confidence interval gives a range of values that includes the outcomes of quantity of interest with a high degree of confidence. It represents the uncertainty band resulting from the input uncertainty. As the uncertainty band derived from the proposed method may be wider or more narrow than the reference, its degree of confidence is higher or smaller than 95%. In order to assess the reliability of the uncertainty band, the equivalent confidence level (ECL) is introduced and evaluated in the way as exemplarily illustrated in Fig. 15. The non-identical CDFs result in inconsistent confidence intervals, e.g., the narrow value range of DS (red) against the wide one of MC (black). The more narrow confidence interval implies a confidence level smaller than 95%. By mapping the lower and upper bounds of the DS confidence interval to the CDF derived from the MC method (indicated by the yellow arrows) and determining the corresponding cumulative probabilities, the ECL can be calculated, which is as expected to be smaller than 95% in Fig. 15.

The ECL is displayed with the orange line in the bottom subplot of Fig. 14. It is expected to be 95% (depicted by the black dotted line), because the confidence level 95% is chosen in current study. As the ECL yields generally high values around 95%, the proposed method produces confidence intervals that quantitatively agree well with the references.

By utilizing the proposed method, the vertical velocity with fluctuating profile is properly handled and the unphysical values after the dissolution of the helium layer are avoided, as exhibited in Figs. 16

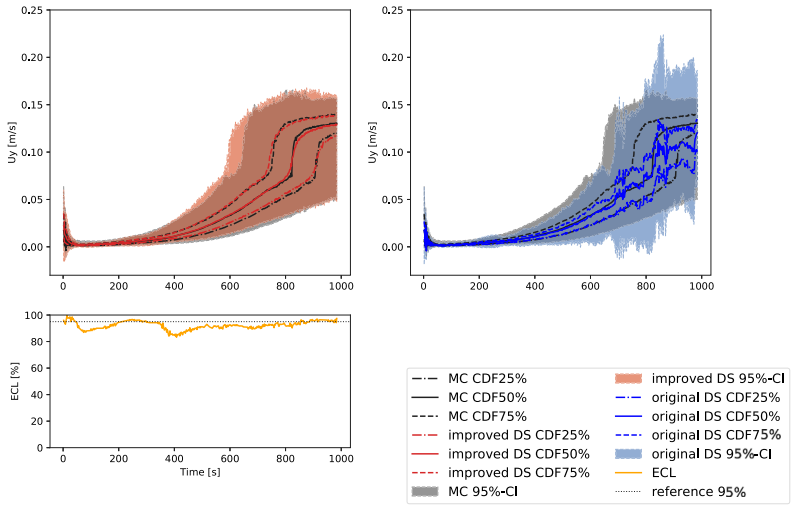

Fig. 16. The 95% confidence intervals and values of U_y at the location (0.015 0.8 0.005) with cumulative probabilities 25%, 50% and 75% obtained with the proposed method (upper left) and the original approach (upper right), both are assessed against the MC results. The evaluation of the 95% confidence intervals obtained with the proposed method by calculating the ECL (bottom left).

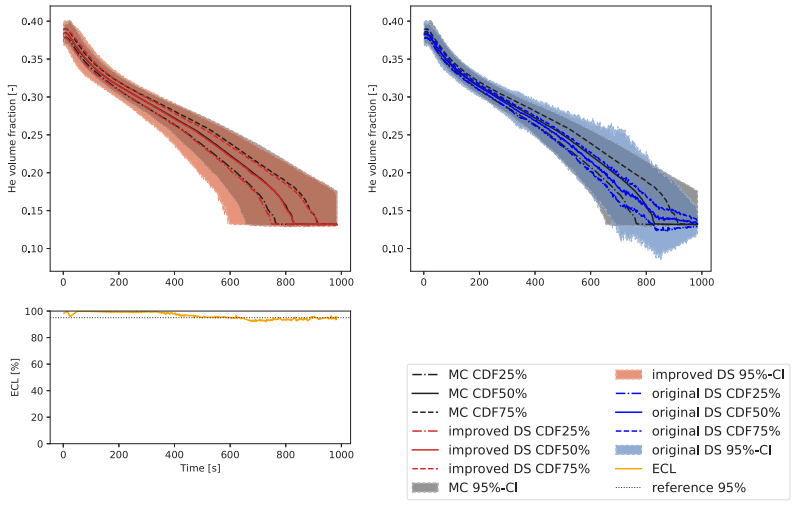

Fig. 17. The 95% confidence intervals and values of the helium concentration at the location (0.125 0.8 0.005) with cumulative probabilities 25%, 50% and 75% obtained with the proposed method (upper left) and the original approach (upper right), both are assessed against the MC results. The evaluation of the 95% confidence intervals obtained with the proposed method by calculating the ECL (bottom left).

and 17. Furthermore, the profiles of both output quantities with different cumulative probabilities are almost identical for the MC and the improved DS approaches (red lines against black lines), because of the similar CDFs as demonstrated in Figs. B.29 and B.30 in Appendix B. The confidence intervals obtained with the proposed method are also in line with the references, with the ECL mostly higher than 90%.

The DS method has been further developed in this work, with the aim to solve the issues of predicting unphysical values and oscillating uncertainty bands. The proposed method enables the generation of a high number of pseudo-outcomes, which can be statistically evaluated to obtain the 95% confidence interval. This yields reasonable profiles for the output uncertainty compared to the reference method MC and is confirmed to be valid. It is hence applied to the technical scale validation case THAI-TH32, which is about the dissolution of an atmospheric stratification due to the natural circulation flow.

4. Application

4.1. Description of the experiment TH32

Fig. 18 left depicts the facility configuration for the TH32 experiment. The stand-alone THAI test vessel (TTV) is made of stainless steel and surrounded by thick mineral wool and thin aluminum for thermal insulation. The large cylindrical part of TTV is designed as a double wall. The gaps between the lower and middle double walls are filled with hot thermal oil for heating the walls, while the one at the upper part is filled with cold oil for the cooling purpose. The large cylindrical part is equally divided into five levels, at which four block flanges are integrated into the TTV. There are two small cylinders at the top and bottom of the vessel, which connect with the large cylindrical part by dish heads. The upper cylinder is covered by a flange with a

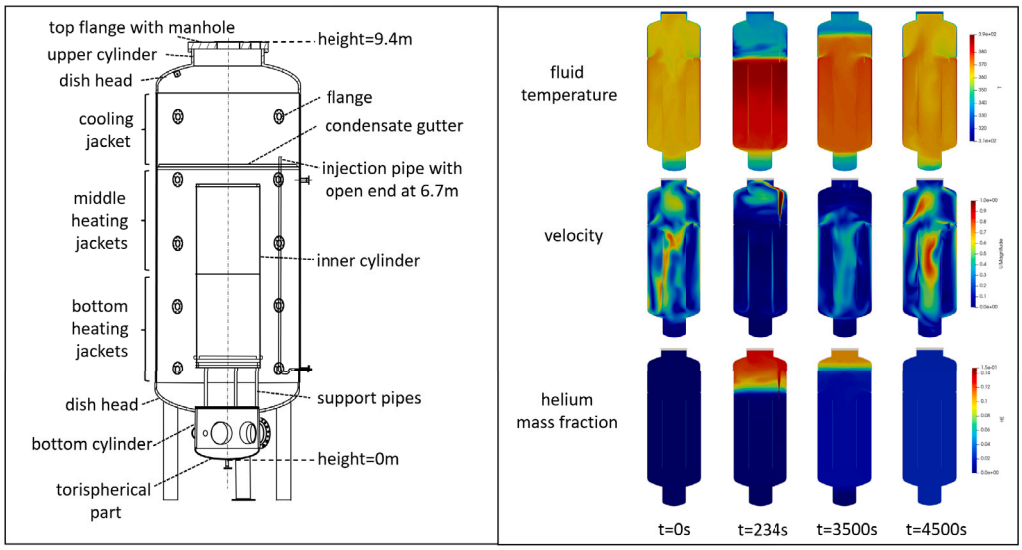

Fig. 18. The test configuration of THAI-TH32 (Freitag et al., 2022a) (left), and the evolution of fluid temperature, velocity and helium mass fraction during the test procedures (right).

manhole on it and the bottom one is closed by a torispherical head. Inside the TTV, the condensate gutters attached to the wall remain, while the condensate trays are removed. An inner cylinder is placed on support rings with six support pipes resting on lower rings. The helium is injected into the vessel atmosphere through a vertically upward directed pipe.

The test conditions were comprehensively described in Freitag et al. (2022a,b). The test procedure consists of the preconditioning phase, the helium injection and mixing phase. The preconditioning phase is intended to establish a large scale natural convection flow in the vessel, driven by the solid structures of different temperatures. As indicated by the velocity in Fig. 18 right, one natural convection flow loop above the inner cylinder and one across the annulus and inner cylinder are identified in the vessel at $t = 0$. In the following procedure, described in Freitag et al. (2022a), cold helium with an average flow rate of 7 g/s is injected into the vessel for around 234 s. The wall and cylinder temperature are slightly affected, while a significant impact on the fluid temperature is observed, i.e., it increases and decreases rapidly at lower and upper sections, respectively. Due to the low density of helium, the light gas is accumulated in the upper section and subsequently suppresses the natural convection flow (see the velocity at $t = 234$ s). At the end of the injection phase, a helium layer is formed above the inner cylinder with increasing helium concentration along the elevation.

After stopping the helium injection, the lower and middle mantles are kept constant in heating mode and upper mantle in cooling mode by providing mostly stable heating/cooling power. Due to the existence of the light gas layer, the flow is suppressed, and weak circulations are observed. The helium layer begins to be diluted from its lower end and then the erosion proceeds upwards. During the erosion of the helium layer, the flow gradually recovers to the initial level. The time for starting the helium injection is recorded as 0 s, the mixing phase ends at 4800 s.

4.2. Simulation setup

For the CFD model, several geometric simplifications have been made, i.e., 20 flange blocks in the TTV, the manholes in the top flange and in the sump compartment and the support structures for the inner cylinder are excluded. Furthermore, the long injection tube is modeled as a resolved nozzle with the open end at the height 6.7 m. The large cylindrical part of TTV is modeled as single-walled. The heating/cooling power supply is represented with a secondary side temperature (T_a) and a heat transfer coefficient (h). The secondary side temperatures of heating/cooling mantles correspond to their averaged thermal oil temperatures, whereas the heat transfer coefficients are calculated according to the heat balance. For the remaining sections at the outer wall, the same type of boundary condition is applied. Their ambient temperatures are defined as those measured in the experimental hall, the heat transfer coefficients are also estimated from heat balance calculations. As for the inner wall of TTV and inner cylinder, their initial temperatures are defined based on the test data that are circumferentially averaged. The conjugate heat transfer (CHT) approach is applied to determine the heat transfer between gas and solid structures (inner wall and inner cylinder). The helium is injected through the lower end of the nozzle by defining its boundary condition as transient mass flow rate and temperature.

The previous considerations and definitions for initial and boundary conditions introduce input uncertainties. The wall temperature is measured and defined with uncertainties, as indicated by the manufacturer of thermocouples or following the circumferentially averaging of all measurements. The heat transfer coefficients are computed based on the heat balance in the initial phase and several assumptions have been made, implying the existence of uncertainties. For the measurement of the helium flow rate, the fluctuation during the helium injection makes the accurate recording challenging and leads to an uncertainty of the total helium mass. As the support structures of the inner cylinder are not considered in the simulation, the reduced solid mass (corresponding to a lower heat capacity) may lead to a faster and higher increase of the cylinder temperature. In order to account for the impact of heat capacity of support structures, the density of the inner cylinder is defined as an uncertain parameter. These considerations result in 14 uncertain parameters, which are specified with uniform distributions, as no value preferences within given uncertainty ranges are justified. They will be further discussed in Section 3.3.

According to the test procedure, the CFD simulation composes four phases, i.e., the preparatory, the initial, the injection and the erosion phases. In the preparatory phase, the calculation is carried out only for the vessel, in order to build the temperature gradient inside the vessel. The remaining three phases follow the test procedure, i.e., the establishment of the natural convection flow induced by differential heating and cooling walls (initial phase), the helium injection (injection phase) and the erosion of the helium stratification (erosion phase).

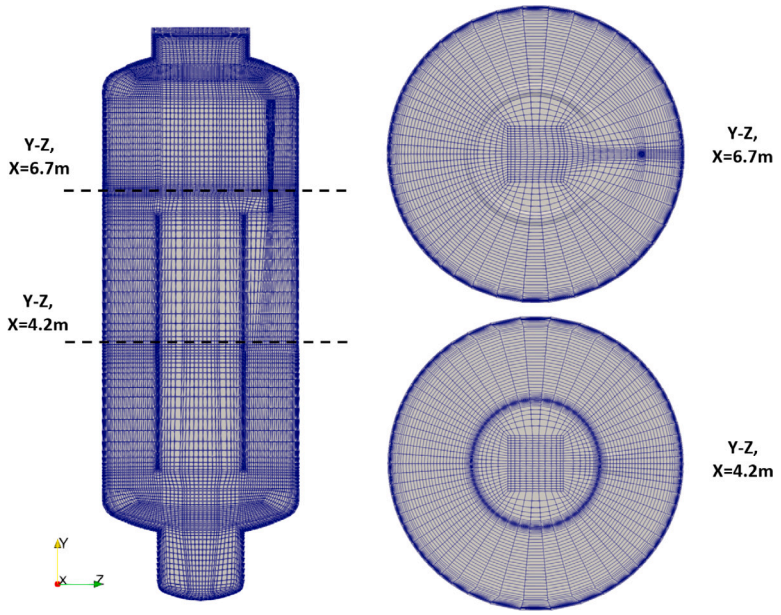

Fig. 19. The mesh for THAI-TH32.

The 3D mesh employed for TH32 is illustrated in Fig. 19. Through a mesh convergence study, a grid with around 1.3 million hexahedral cells was identified yielding reasonable accuracy and thus is used for following simulations. It is noted that the wall boundary layers are resolved with an average $y^+ < 2$ to avoid using wall functions, as suggested in Kumar et al. (2020). The numerical schemes used are second-order accurate.

The *containmentFOAM* solver, a tailored solver and model library based on *OpenFOAM*®, is applied with the governing equations explained in detail in Kelm et al. (2021). In contrast to the previous simulations, the current one extensively models the heat exchange at the interface between fluid and solid domains with the conjugate heat transfer method, which requires solving an additional energy equation in the solid domain. The equations used to calculate the flow in the vessel remain the same. The mixture transport properties (the kinematic viscosity and thermal conductivity) are determined with the Wilks' mixture model, whereas the mixture specific heat capacity is calculated with the mass fraction weighted sum of each species' specific heat capacity. As for the determination of the diffusive transport of helium in air, the Fuller binary diffusion model is employed. In addition, the radiation heat transfer is considered. Since the fluid (dry air dominant and helium) does not participate in the radiation (Kumar et al., 2020), only the surface-to-surface radiation heat transfer is modeled with the finite volume Discrete Ordinates Method (fvDOM).

4.3. Results for input uncertainty propagation

14 uncertain parameters assigned with uniform distributions were defined. Through a sensitivity study, seven of them were identified as significant and considered for the UQ, as shown in Fig. 20. For the uncertainty analysis, eight binary samples were generated with the same matrix depicted in Table 2. As relevant output quantities, the transient wall temperature, the fluid temperature, the velocity and the helium concentration (typically used for validation) are evaluated.

The quantity Y_{ref} used to determine a unique physical state that could be used for the mapping (similar as in Fig. 10) is defined with the following equation:

$$Y_{ref} = \sqrt{\frac{\int_V w_{he,i}^2 \mathrm{d}V}{V_{tot}}}, \tag{8}$$

where $w_{he,i}$ is the helium mass fraction at each cell and V_{tot} the total volume of the fluid domain. The behavior of Y_{ref} is illustrated in Fig. 21. It ramps up during the helium injection and then decreases gradually during the mixing process. For this reason, the UQ analysis has been carried out with the proposed method for the injection and erosion phases separately. The obtained 95% confidence intervals are then merged together and assessed against the test data.

The formation of the helium layer and its erosion are represented by measuring the helium concentration at different locations. Fig. 22 depicts the evolution of helium concentration in the dome, with the blue and red areas indicating the 95% confidence intervals obtained with the original and improved DS methods, respectively. The red lines with different styles are the helium concentrations with the cumulative probabilities 25%, 50% and 75%. As demonstrated in Fig. 18, the erosion of the helium stratification proceeds upwards. Before the convective erosion front reaches the sensor position, there is a stagnant phase, where the helium is transported mainly by diffusion. Afterwards, the helium layer is dissolved efficiently by the global convective mixing process. A similar behavior is observed in the simulation, however the onset of the convective erosion (sharp drop of helium concentration) is predicted with a time delay.

This can be explained by the velocity in the annulus, as shown in Fig. 23. Compared to the experiment, the completely suppressed flow cannot contribute to the helium transport to the lower part of the vessel, leading to a longer stagnant phase and the extension of the erosion phase in the simulation. Despite this, both uncertainty bands for the helium concentration and the velocity are reasonably represented using the proposed method, i.e., the unphysical 'overshoots' before and after the convective erosion are excluded (Fig. 22) and the velocity characterized with an oscillatory profile is adequately treated (Fig. 23).

The wall and fluid temperatures in the annulus are further evaluated, as exhibited in Figs. 24 and 25. They imply the heat transfer

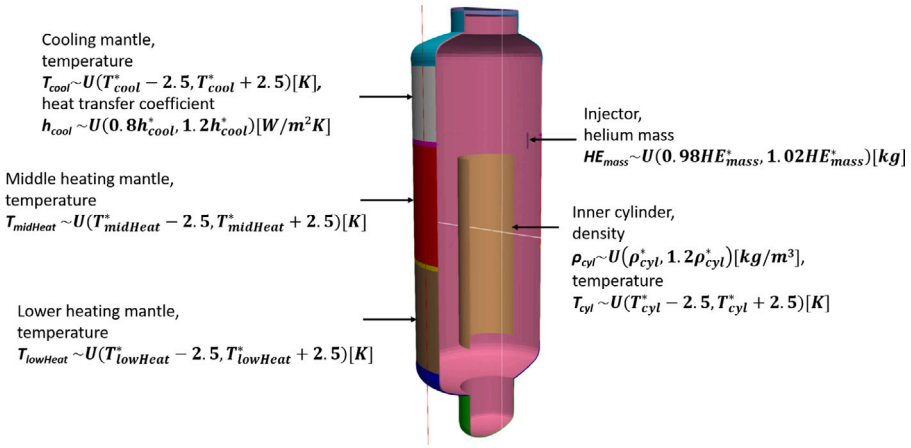

Fig. 20. The seven uncertain parameters assigned with uniform distributions. Symbols marked with an asterisk correspond to nominal values.

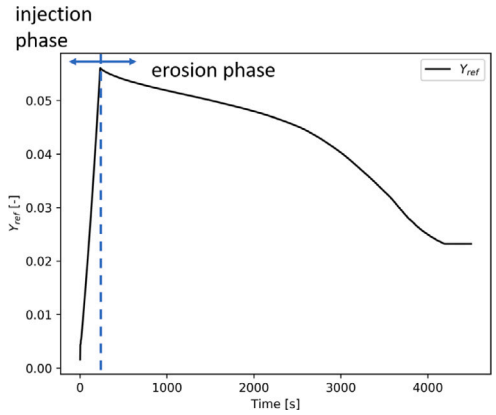

Fig. 21. The behavior of Y_{ref} in the injection and erosion phases.

between the wall and fluid, which is the driving force of the flow in the vessel. The fluid temperature is overestimated and the temperature difference between the wall and fluid is smaller than the measurements, indicating a reduced heat exchange and thus a smaller driving force for the flow.

Based on the preceding analysis, it is summarized that the simulation reproduces qualitatively the experimental phenomena, however the investigated uncertainties of the input parameters do not explain the deviation from the experiment, in particular the longer stagnant phase. Additionally, the impact of the turbulence modeling approach URANS has been assessed in a parallel work with the LES turbulence closure (Ji et al., 2023a), which did not yield a significant influence. The possible reasons seem to be the simplifications made in the simulation. For instance, instead of an asymmetrical wall temperature distribution at the inner vessel wall, a uniform wall temperature in circumferential direction is applied. Furthermore, the internal structures, e.g. support structures for the inner cylinder and instrumentation are excluded. They may induce local turbulence, instabilities and represent heat sinks causing buoyancy flow accelerating the mixing process. For further investigation, more efforts need to be taken to impose 3D boundary conditions and define a refined geometry.

The proposed method for input uncertainty propagation yields more realistic output uncertainty bands, and the computational effort for a technical-scale validation case is reasonable with currently eight parametric runs.

5. Conclusions

The transport and mixing of flammable gases in the containment and the potential combustion of a flammable gas cloud are of high safety relevance. The experiment TH32, conducted by Becker Technologies GmbH, investigates buoyancy-driven flow and hydrogen distribution on a technical scale. To gain more detailed insights into the complex 3D flow and mixing processes, CFD models are utilized. However, the reliability of these CFD simulations is affected by various sources of uncertainties, including numerical, model, and input uncertainties. This work specifically addresses the input uncertainty.

Various uncertainty quantification (UQ) methods are available to quantify the influence of input uncertainties on CFD simulations. This study investigates the deterministic sampling (DS) method due to its computational efficiency and effectiveness in nuclear reactor safety applications. To derive output uncertainty, an assumption about the probability density function is necessary, in addition to the computed output statistics (e.g., mean value, standard deviation, and higher statistical moments). The common assumption of a normal distribution often leads to predictions of unphysical values and poor representation of output uncertainties, particularly for parameters with chaotic behavior. To address these issues, a new method has been developed that generates reasonable pseudo-outcomes, from which cumulative density functions and 95% confidence intervals can be derived. This proposed method has been assessed against the Monte Carlo (MC) sampling approach using a simple test case, requiring eight DS samples and 500 MC samples for seven uncertain parameters. The derived output uncertainties eliminate unphysical values, and parameters with fluctuating profiles are properly evaluated. Furthermore, the output uncertainties show good agreement with reference values.

After confirming the reliability of the proposed method, it was applied to the validation case TH32, which represents a buoyancy-driven mixing transient. The UQ analysis required eight CFD simulations considering seven uncertain input parameters. The quantities of helium concentration, velocity, and wall and fluid temperature were evaluated, and their 95% confidence intervals were derived and compared against the test data. The proposed method produced more realistic output uncertainties, exhibiting profiles similar to the measurements. Consequently, it is feasible to conduct UQ for the current application with reasonable computational effort. Through the assessment of simulation results against the test data, notable deviations were identified, implying the existence of epistemic uncertainties that require further investigation.

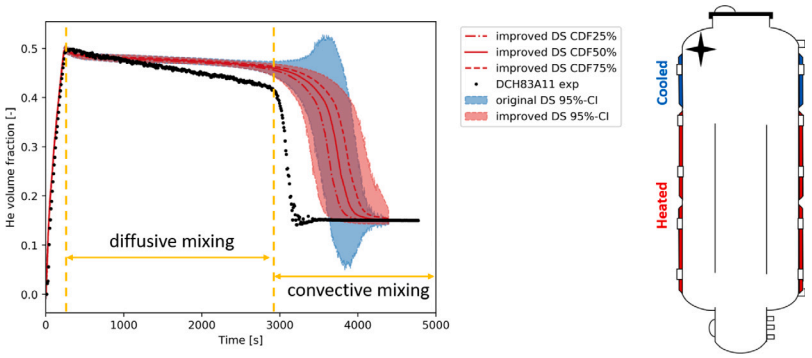

Fig. 22. The output uncertainties for the helium concentration in the dome, derived with the proposed and original methods.

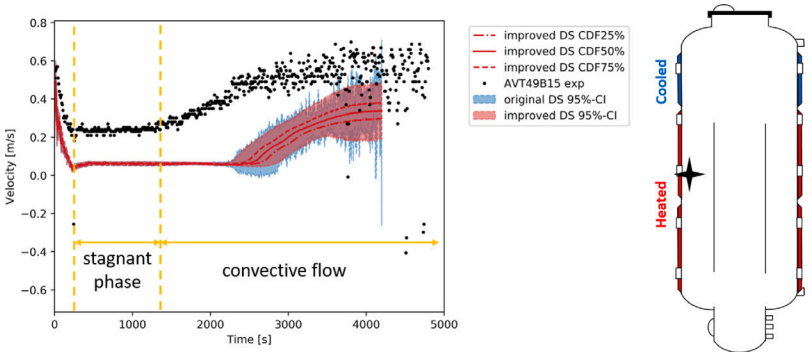

Fig. 23. The output uncertainties for the velocity near the middle heated wall, derived with the proposed and original methods.

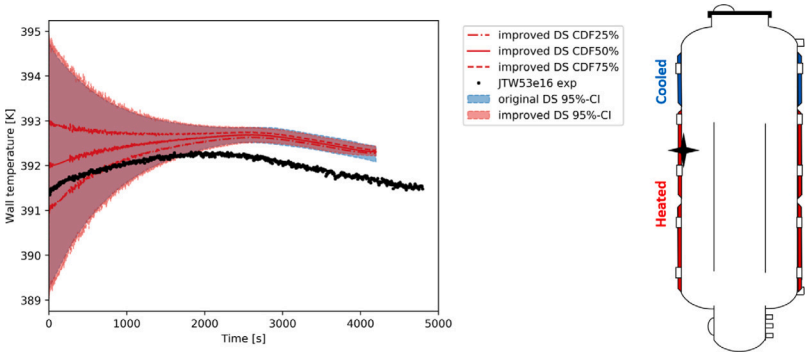

Fig. 24. The output uncertainties for the wall temperature at the middle heating jacket, derived with the proposed and original methods.

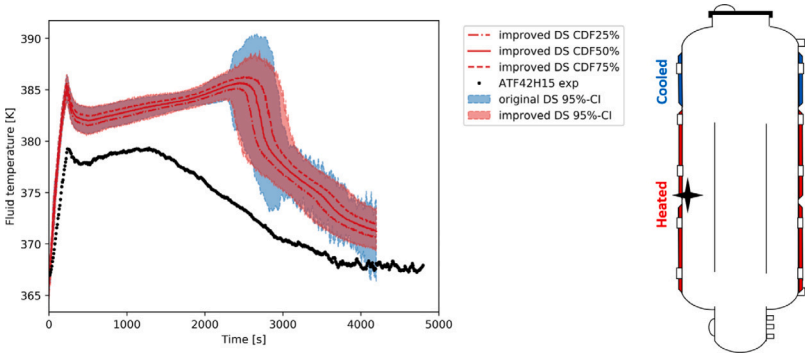

Fig. 25. The output uncertainties for the fluid temperature in the annulus, derived with the proposed and original methods.

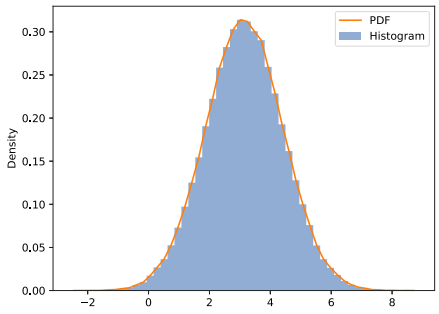

Fig. A.26. The histogram and PDF derived from a set of sample data.

CRediT authorship contribution statement

Ruiyun Ji: Writing – review & editing, Writing – original draft, Methodology, Investigation. **Stephan Kelm:** Writing – review & editing, Supervision. **Markus Klein:** Writing – review & editing, Supervision.

Declaration of competing interest

The authors declare that they have no known competing financial interests or personal relationships that could have appeared to influence the work reported in this paper.

Data availability

The authors do not have permission to share data.

Acknowledgments

The presented project was conducted in close cooperation between the University of the Bundeswehr Munich and Forschungszentrum Jülich. The authors gratefully acknowledge the funding by the German Federal Ministry for the Environment, Nature Conservation, Nuclear Safety and Consumer Protection (BMUV) on the decision of the German Bundestag (Project number 1501595).

The computational resources for the URANS simulations have been granted by the Gauss Centre for Supercomputing/Leibniz Supercomputing Centre (project ID pn29ce) and the Jülich Supercomputing Centre (project IDs uq4cfd and cfrun).

The authors acknowledge Becker Technologies GmbH for carefully conducting, documenting and sharing the experimental data of the experiment THAI-TH32.

Appendix A. The statistical analysis on samples

The PDF describes the likelihood of a random variable taking on a particular value within a given range. It can be derived from the gathered data, as illustrated in Fig. A.26. The probability information represented by the PDF is expressed with $f(Y) = P(Y)$, where Y stands for a random variable.

The CDF (denotes as $F(Y)$) represents the cumulative probabilities that a random variable Y is less than or equal to a specified value Y_i (Fig. A.27), with the expression $F(Y) = P(Y \leq Y_i)$. It starts at 0 and reaches 1 for the smallest and largest possible values, respectively. The CDF is particularly useful in computing probabilities for intervals, such as the 95% confidence interval, which is used to present the output uncertainty in this work.

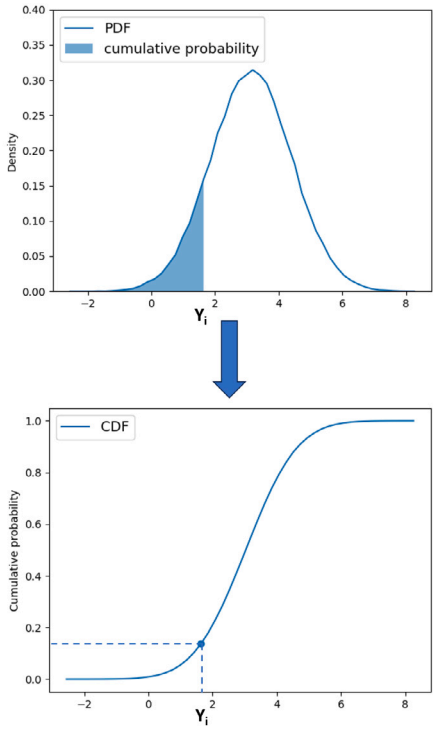

Fig. A.27. The derivation of cumulative probability from the PDF.

The 95% confidence interval is determined by finding the values Y_a and Y_b fulfilling the condition:

$$F(Y_b) - F(Y_a) = P(Y_a \leq Y \leq Y_b) = 0.95. \tag{A.1}$$

In general, the critical values Y_a and Y_b with $F(Y_a)$ close to 2.5% and $F(Y_b)$ close to 97.5% are chosen, corresponding to the lower and upper bounds of the 95% confidence interval. It implies that, the probability of Y falling within the interval $[Y_a, Y_b]$ is 95%.

Appendix B. The CDFs derived from the proposed method with comparison to those from the MC approach

See Figs. B.28–B.30

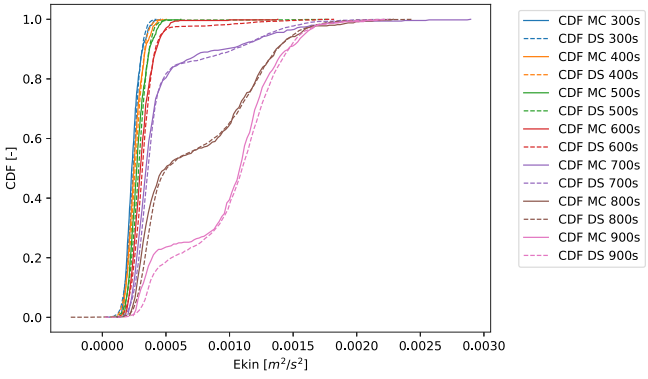

Fig. B.28. The CDFs derived with the MC approach and the proposed method for E_{kin} at various times.

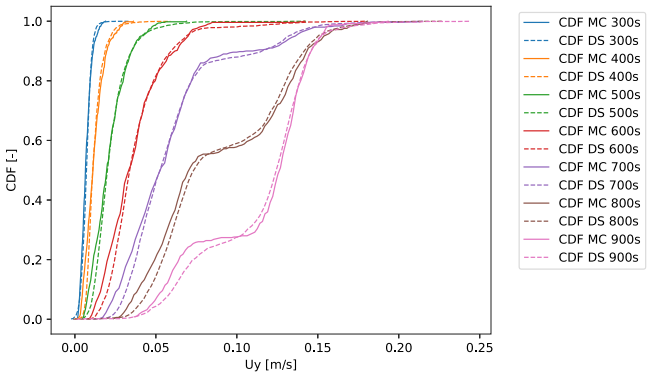

Fig. B.29. The CDFs derived with the MC approach and the proposed method for the vertical velocity at various times.

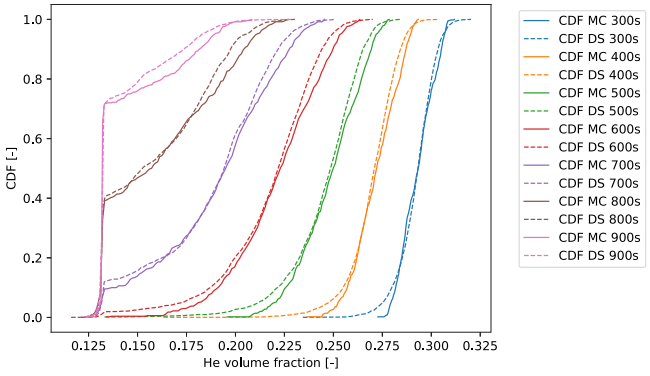

Fig. B.30. The CDFs derived with the MC approach and the proposed method for the helium concentration at various times.

References

Abe, S., Ishigaki, M., Sibamoto, Y., Yonomoto, T., 2015. RANS analyses on erosion behavior of density stratification consisted of helium–air mixture gas by a low momentum vertical buoyant jet in the PANDA test facility, the third international benchmark exercise (IBE-3). Nucl. Eng. Des. 289, 231–239.

Angrisani, L., D'Apuzzo, M., Moriello, R.S.L., 2005. The unscented transform: a powerful tool for measurement uncertainty evaluation. In: Proceedings of the 2005 IEEE International Workshop on Advanced Methods for Uncertainty Estimation in Measurement. IEEE, pp. 27–32.

Blatman, G., Sudret, B., 2011. Adaptive sparse polynomial chaos expansion based on least angle regression. J. Comput. Phys. 230 (6), 2345–2367.

Dudley, R., 2012. The shapiro-wilk test for normality. Available online: URL: https://math.mit.edu/~rmd/46512/shapiro.pdf.

Eça, L., Hoekstra, M., 2014. A procedure for the estimation of the numerical uncertainty of CFD calculations based on grid refinement studies. J. Comput. Phys. 262, 104–130.

Freitag, M., Schmidt, E., Colombet, M., von Laufenberg, B., Kühnel, A., 2022a. Evaluation of Experimental Uncertainties in Tests with Light Gas Stratifications and Their Dissolution by Natural Convection Tests TH-30-32. Technical report, Becker Technologies GmbH.

Freitag, M., Schmidt, E., Schramm, B., Stewering, J., Kelm, S., Janda, T., Kotouč, M., Povilaitis, M., Lane, J.W., Winter, S.D., George, T.L., Hoffrichter, J., Koch, M., Kljenak, I., 2022b. Simulation benchmark based on the THAI-experiment on generation and dissolution of a light gas stratification by natural convection. In: 19th International Topical Meeting on Nuclear Reactor Thermal Hydraulics. NURETH-19, Brussels, Belgium, March 6 - 11.

Glaeser, H., 2008. GRS method for uncertainty and sensitivity evaluation of code results and applications. Sci. Technol. Nucl. Installations 2008.

Gupta, S., Schmidt, E., Von Laufenberg, B., Freitag, M., Poss, G., Funke, F., Weber, G., 2015. THAI test facility for experimental research on hydrogen and fission product behaviour in light water reactor containments. Nucl. Eng. Des. 294, 183–201.

Hessling, J.P., 2013. Deterministic sampling for propagating model covariance. SIAM/ASA J. Uncertain. Quant. 1 (1), 297–318.

Ji, R., Wenig, P.J., Kelm, S., Klein, M., 2023. Epistemic uncertainty in URANS based CFD analysis of buoyancy driven flows — Comparison of URANS and LES. Ann. Nucl. Energy 181, 109563.

Ji, R., Wenig, P., Kelm, S., Klein, M., 2023a. Development and assessment of the uncertainty analysis for the URANS based CFD simulations. Technical report, GRS, Reactor Safety Research, Project-No. 1501595.

Julier, S.J., Uhlmann, J.K., 2004. Unscented filtering and nonlinear estimation. Proc. IEEE 92 (3), 401–422.

Kelm, S., Kampili, M., Liu, X., George, A., Schumacher, D., Druska, C., Struth, S., Kuhr, A., Ramacher, L., Allelein, H.J., Prakash, K.A., 2021. The tailored CFD package 'containmentFOAM' for analysis of containment atmosphere mixing, H2/CO mitigation and aerosol transport. Fluids 6 (3), 100.

Kelm, S., Lehmkuhl, J., Jahn, W., Allelein, H.-J., 2016. A comparative assessment of different experiments on buoyancy driven mixing processes by means of CFD. Ann. Nucl. Energy 93, 50–57.

Kumar, G.V., Kampili, M., Kelm, S., Prakash, K.A., Allelein, H.-J., 2020. CFD modelling of buoyancy driven flows in enclosures with relevance to nuclear reactor safety. Nucl. Eng. Des. 365, 110682.

Mahaffy, J., Chung, B., Song, C., Dubois, F., Graffard, E., Ducros, F., Heitsch, M., Scheuerer, M., Henriksson, M., Komen, E., Moretti, F., 2015. Best Practice Guidelines for the Use of CFD in Nuclear Reactor Safety Applications-Revision. Technical report, Organisation for Economic Co-Operation and Development.

Menter, F.R., Kuntz, M., Langtry, R., 2003. Ten years of industrial experience with the SST turbulence model. Turbul. Heat and Mass transf 4 (1), 625–632.

Pisaroni, M., 2017. Multi level Monte Carlo methods for uncertainty quantification and robust design optimization in aerodynamic (Ph.D. thesis). EPFL.

Rakhimov, A.C., Visser, D., Komen, E., 2019. Uncertainty quantification method for CFD applied to the turbulent mixing of two water layers–II: Deterministic sampling for input uncertainty. Nucl. Eng. Des. 348, 146–158.

Shaphiro, S., Wilk, M., 1965. An analysis of variance test for normality. Biometrika 52 (3), 591–611.

Smith, R.C., 2013. Uncertainty Quantification: Theory, Implementation, and Applications. vol. 12, SIAM.

Smith, B., Andreani, M., Bieder, U., Ducros, F., Bestion, D., Graffard, E., Heitsch, M., Scheuerer, M., Henriksson, M., Hoehne, T., Houkema, M., 2015. Assessment of CFD Codes for Nuclear Reactor Safety Problems - Revision 2. Technical Report, Organisation for Economic Co-Operation and Development.

Wang, W., Ma, W., 2023. Application of deterministic sampling methods to uncertainty quantification in MELCOR severe accident simulation. Nucl. Eng. Des. 403, 112121.

Wenig, P.J., Ji, R., Kelm, S., Klein, M., 2021. Towards uncertainty quantification of LES and URANS for the buoyancy-driven mixing process between two miscible fluids — Differentially heated cavity of aspect ratio 4. Fluids 6 (4), 161.

Wenig, P.J., Kelm, S., Klein, M., 2023. CFD uncertainty quantification using stochastic spectral methods — Exemplary application to a buoyancy-driven mixing process. Nucl. Eng. Des. 409, 112317.